

1 Aged boreal biomass burning aerosol size distributions from 2 BORTAS 2011

3

4 K.M. Sakamoto^{1,2}, J. D. Allan³, H. Coe³, J. W. Taylor³, T. J. Duck², J. R. Pierce^{1,2}

5

6 [1] Colorado State University, Fort Collins, CO, USA

7 [2] Department of Physics and Atmospheric Science, Dalhousie University, Halifax, NS, CAN

8 [3] University of Manchester, Manchester, UK

9

10 Corresponding author: J.R. Pierce (jeffrey.pierce@colostate.edu)

11

12 Abstract

13

14 Biomass-burning aerosols contribute to aerosol radiative forcing on the climate system. The magnitude
15 of this effect is partially determined by aerosol size distributions, which are functions of source fire
16 characteristics (e.g. fuel type, MCE) and in-plume microphysical processing. The uncertainties in
17 biomass-burning emission number size-distributions in climate model inventories lead to uncertainties
18 in the CCN concentrations and forcing estimates derived from these models.

19 The BORTAS-B measurement campaign was designed to sample boreal biomass-burning
20 outflow over Eastern Canada in the summer of 2011. Using these BORTAS-B data, we implement
21 plume criteria to isolate the characteristic size-distribution of aged biomass-burning emissions (aged ~
22 1 – 2 days) from boreal wildfires in Northwestern Ontario. The composite median size-distribution
23 yields a single dominant accumulation mode with $D_{pm} = 230$ nm (number-median diameter); and $\sigma =$
24 1.75, which are comparable to literature values of other aged plumes of a similar type. The organic
25 aerosol enhancement ratios ($\Delta OA/\Delta CO$) along the path of Flight b622 show values of 0.095-0.178 μg
26 m^{-3} $ppbv^{-1}$ with no significant trend with distance from the source. This lack of enhancement ratio
27 increase/decrease with distance suggests no detectable net OA production/evaporation within the aged
28 plume over the sampling period (plume age: 1-2 days), though does not preclude OA production/loss at
29 earlier stages.

30 A Lagrangian microphysical model was used to determine an estimate of the freshly emitted

31 size distribution corresponding to the BORTAS-B aged size-distributions. The model was restricted to
32 coagulation and dilution processes based on the insignificant net OA production/evaporation derived
33 from the $\Delta\text{OA}/\Delta\text{CO}$ enhancement ratios. We estimate that the *youngfresh*-plume median diameter was
34 in the range of 59-94 nm with modal widths in the range of 1.7-2.8 (the ranges are due to uncertainty in
35 the entrainment rate). Thus, the size of the freshly emitted particles is relatively unconstrained due to
36 the uncertainties in the plume dilution rates.

37

38 **1. Introduction**

39 **1.1 Biomass burning particles**

40 Biomass burning is a significant emission source of carbonaceous aerosols to the global atmosphere
41 (Andreae and Merlet, 2001; Reid et al., 2005). In addition to releasing high levels of greenhouse gases
42 (CO_2 , CO) and volatile organic compounds, biomass burning releases smoke particles that have climate
43 impacts through the direct and indirect aerosol effects. These particles are primarily composed of a
44 mixture of black carbon and organic carbon, with inorganics contributing some mass (Capes et al.,
45 2008; Carrico et al., 2010; Cubison et al., 2011; Hecobian et al., 2011; Hennigan et al., 2011; Hudson et
46 al., 2004; Reid et al., 2005). These particles directly affect the Earth's radiation balance and climate by
47 scattering and absorbing incoming solar radiation (Haywood, 2000; Jacobson, 2001). Biomass
48 burning particles may also act as cloud condensation nuclei (CCN) and affect climate and radiation
49 through modifying cloud albedo and lifetime (Pierce et al., 2007; Spracklen et al., 2011) (indirect
50 aerosol effects). Globally, the direct and indirect climate effects represent the largest uncertainties in
51 radiative forcing as quantified by the recent IPCC report (Myhre et al., 2013), and biomass burning
52 emissions represent significant contributions to each of the effects globally (Alonso-Blanco, 2014; Lee
53 et al., 2013).

54 The size of biomass-burning particles (and all particles in general) can have large impacts on
55 the magnitude of these direct and indirect effects (Lee et al., 2013; Seinfeld and Pandis, 2006;
56 Spracklen et al., 2011). Regarding the direct effect, the mass-scattering and mass-absorption
57 efficiencies (the amount of scattering and absorption per mass of aerosol particles) depend on the size
58 of the particles, so errors in the predicted/assumed values of biomass-burning particle size may lead to
59 errors in simulated direct aerosol climate effects (Seinfeld and Pandis, 2006). Regarding the indirect
60 effect, particles that are larger in diameter and more hygroscopic are more likely to act as CCN (Petters
61 and Kreidenweis, 2007). Typically particles larger than 30-100 nm act as CCN depending on

62 conditions and hygroscopicity (Petters and Kreidenweis, 2007; Petters et al., 2009), though this range
63 may be slightly larger ~~or smaller sizes~~ for ~~fresh-~~ fresh biomass-burning particles due to these particles
64 being initially ~~more hydrophobic/~~hydrophilic (depending on fuel type) than typical ambient aerosol-
65 (Carrico et al., 2010; Engelhart et al., 2012; Petters and Kreidenweis, 2007). Furthermore, for constant
66 emissions mass, a factor-of-2 change in diameter, leads to a factor-of-8 change in number emissions,
67 which may contribute to significant changes in CCN concentrations (Pierce et al., 2007; Spracklen et
68 al., 2011). Thus, it is important to provide accurate emissions sizes from biomass burning sources to
69 atmospheric aerosol models looking at aerosol-climate interactions. Lee et al. (2013) found that
70 uncertainties in biomass-burning aerosol emission diameter were responsible for large uncertainties in
71 CCN concentrations in the GLOMAP model (third largest CCN sensitivity out of 28 globally).

72 Atmospheric processing causes the physical and chemical properties of biomass-burning (BB)
73 aerosol evolve over time. These processes have an effect on the size and composition of the particles,
74 and thus influence their direct and indirect effects. Coagulation is a driving factor in size-distribution
75 evolution due to the high concentrations of particles within plumes (Andreae and Merlet, 2001; Capes
76 et al., 2008). Production of secondary organic aerosol (SOA) in-plume has been observed in chamber
77 studies (Cubison et al., 2011; Grieshop et al., 2009; Hennigan et al., 2011; Heringa et al., 2011; Ortega
78 et al., 2013) and in the field (DeCarlo et al., 2010; Lee et al., 2008; Reid et al., 1998; Yokelson et al.,
79 2009), and this SOA will condense onto the particles growing them to larger sizes. In addition, the
80 primary organic aerosol (POA) emitted by the fires may evaporate during the dilution of the plume
81 (Huffman et al., 2009; May et al., 2013; Hennigan et al., 2011). Finally, new particle formation in
82 smoke plumes has been observed in smog chamber studies (Hennigan et al., 2012) as well as in the
83 field (Andreae et al., 2001; Hobbs et al., 2003; Rissler et al., 2006).

84 In global and regional modeling of biomass-burning aerosols, mass-based biomass-burning
85 inventories are the standard, and are generally not accompanied by size data (Reid et al., 2009; van der
86 Werf et al., 2010; Wiedinmyer et al., 2011), leaving size-distribution estimates to the individual
87 investigator. Current global and regional atmospheric aerosol models have gridbox spatial scales
88 (10s-100s of kms) much larger than many initial biomass-burning plume widths (<10 km). This means
89 that sub-grid aging of aerosol plumes by microphysical processes (coagulation,
90 condensation/evaporation and nucleation) processes will lead to changes in the size distribution that the
91 models cannot explicitly resolve. Therefore, the biomass-burning emissions size distributions must be
92 aged distributions that already account for sub-grid processes. Quantifying the natural variations in

93 biomass-burning aerosols are therefore necessary for accurate predictions. Previous studies of field and
94 lab experiments show biomass burning size-distributions vary according to plume age, combustion
95 phase, and fuel type (Adler et al., 2011; Capes et al., 2008; Hobbs et al., 2003; Hennigan et al., 2011;
96 Hosseini et al., 2010; Janhäll et al., 2010; MeMeeking et al., 2009; Okoshi et al., 2014). A review of
97 observed size distribution data by Janhäll et al. (2010) showed the differences in modal width and
98 median diameter as a function of fuel type (forest, savannah, grass), modified combustion efficiency,
99 and plume age (fresh versus aged). CombustionSmog chamber experiments in the FLAME lab have
100 demonstrated similar fuel-type differences in fresh BB size-distributions (Levin et al., 2010).

101 Due to the combination of emission and atmospheric processing factors contributing to the
102 evolution of the BB aerosol size-distribution, characterization of observed, aged BB aerosol is valuable.
103 Adding to the database of observations helps constrain the uncertainties associated with aerosol size.
104 Thus, to improve biomass-burning-aerosol/climate interactions in models, there is a need to
105 characterize the size of particles in aging and aged biomass-burning plumes for a range of fire types
106 and atmospheric conditions (Bauer et al., 2010; Chen et al., 2010; Lee et al., 2013; Pierce et al., 2007;
107 Reddington et al., 2011; Spracklen et al., 2011). In this paper, we specifically investigate the size
108 distributions measured in aged plumes (1-2 days) of large boreal forest fires over Canada.

109 In this paper, we analyze size-distribution and organic aerosol data from BORTAS-B flights that
110 sampled highly concentrated smoke plumes over Eastern Canada on July 20-21st, 2011. A brief
111 overview of the BORTAS-B campaign, instrumentation, and source fire conditions are provided in
112 Section 2.1-2.2. A description of the quantitative plume criteria used to determine plume (versus out of
113 plume) sampling periods is found in Section 2.3. In addition to observational data, we use an
114 aerosol-microphysics box model to simulate the microphysical evolution of number size-distributions.
115 This model was employed to estimate the likely youngfresh-plume size distribution associated with the
116 source fires sampled by BORTAS-B. A full model description is provided in Section 2.4. We present
117 the BORTAS-B research flight results in Section 3, which include the measured aged size distributions,
118 evidence for/against net OA production, and the aging simulations. Finally, we provide conclusions in
119 Section 4.

120

121 **2. Methods**

122 **2.1 BORTAS overview**

123 The *Quantifying the impact of Boreal forest fires on the Tropospheric oxidants over the Atlantic using*

124 *Aircraft and Satellites* (BORTAS-B) measurement campaign was held in Eastern/Atlantic Canada from
125 July 11 – August 3, 2011 (Palmer, 2013). The goal was to characterize pyrogenic outflow from boreal
126 forest wildfires using a variety of sampling and observational techniques with emphasis on plume
127 photochemical evolution. ~~BORTAS-B was the second phase of a collaborative effort between UK and~~
128 ~~Canadian groups after a less intensive BORTAS-A campaign took place over the same geographical~~
129 ~~area in 2010 (Palmer, 2013).~~

130 BORTAS-B incorporated predictive chemical transport modelling (GEOS-Chem), satellite
131 observations, a ground-based in-situ network of sondes (Environment Canada) and ground-base
132 samplers and profilers (Dalhousie Ground Station, DGS), and the UK Facility for Airborne
133 Atmospheric Measurements Airborne Research Aircraft (FAAM-ARA) for inflight sampling. For a
134 complete overview of the BORTAS-B set-up and instrumentation, see (Palmer, 2013). The ARA flew
135 fourteen research flights over the campaign period.

136 The flight paths of the ARA flights that we analyze in this paper can be seen in Figure 1. Flights
137 BAE-b622 and BAE-b623 were research flights between Halifax, NS and Sherbrooke, QB spanning
138 July 20-21, 2011. They flew ascent and descent patterns (ranging ~1-7 km ASL) to sample vertical and
139 horizontal transects in regions forecasted to contain biomass-burning plumes. These flights were
140 selected because they were roughly co-located and back-to-back, increasing the likelihood of sampling
141 similar outflow and allowing for a common plume criteria to be applied across both flights. They also
142 contained the majority of ~~the~~ biomass-burning aerosol ~~sampling~~ during the 14-flight campaign.

143 In addition, Flight b622 sampled along a relatively straight path to/from the fires that allowed
144 for analysis of the evolution of plume aerosol properties (Flight b623 had a much more complicated
145 and compact sampling path so we did not use this flight to determine the evolution of aerosol
146 properties). We have divided these flights into vertical transects by ascent/descent with the midpoints
147 transect represented in Figure 1.

148 The sampled wildfire plumes originated from intense regional fires near the Northwestern
149 Ontario-Manitoba border (centred 52° N, 93° W). The MODIS hotspots in Figure 1 show a number of
150 intense fires (fire radiative power >100 MW) in northwestern Ontario for the three days prior to the
151 analyzed flights (June 17-20, 2011). According to the Ontario Ministry of Natural Resources, Ontario
152 experienced one of its worst fire seasons in terms of burned area with 635,374 hectares burned in 2011.
153 ~~This is significantly greater than the acreage burned in 2010 during the BORTAS-A campaign (15,000~~
154 ~~hectares).~~The abundance of individual fires in a relatively large source region lead to mixed

155 combustion phases and dominant hotspots over the course of the campaign. A combination of flaming
156 and smouldering phases were reported by Natural Resources Canada with primary fuels consisting of
157 jack pine (*pinus banksiana*) and black spruce (*picea mariana*) throughout the fire region (Ontario
158 ministry of natural resources: 2011 forest summary).

159 The dominant west-east climatological meteorology during the BORTAS-B campaign allowed
160 the biomass-burning emissions from these fires to be transported downwind over the ground-base,
161 (DGS) in Halifax, NS (44.5° N, 63.1° W). The plumes intersected by flights b622 and b623 had a
162 physical transport age estimated through HYSPLIT backtrajectories of between 1-2 days as
163 summarized in Table 1. The backtrajectory analysis (not shown) shows air masses passing over the
164 biomass-burning region later being intersected by the flight paths at varying altitudes. ~~—; however,~~
165 ~~this is different than the time since passing over the fire region because the photochemical age includes~~
166 ~~the photochemical age of air mixed into the plume calculated by Palmer et al. (2013) to be 1-5 days for~~
167 ~~b622 and 2-4 days for b623 as~~ The estimated photochemical age of the plumes, based on non-methane
168 hydrocarbon analysis via Parrish et al. (2007) w The estimated photochemical age of the plumes,
169 calculated by Palmer et al. (2013) (by non-methane hydrocarbon analysis; Parrish et al. (2007)), were
170 1-5 days for b622 and 2-4 days for b623. These estimates may be longer than the physical transport
171 ages due to the entrainment of background air (which is more photochemically aged) into the plumes.

172

173 **2.2 ARA Instrumentation**

174 The ARA aircraft was outfitted with instruments designed for sampling chemical and physical
175 characteristics of biomass-burning outflow. Gaseous and particulate in-flight sampling was
176 accomplished across a suite of instruments; the relevant instruments for this study are described below.
177 A full description of all payload instruments can be found in (Palmer, 2013).

178 The suite of instruments on the ARA included measurements of multiple gaseous
179 biomass-burning tracers. Carbon monoxide (CO) mole fraction was measured via VUV Fast
180 fluorescence CO analyzer averaged over 1s (3% estimated accuracy). Acetonitrile (CH₃CN), a
181 biomass-burning marker VOC associated with plant pyrolysis, was measured along with a number of
182 other VOCs with a proton-transfer-reaction mass spectrometer (PTR-MS) system (co: University of
183 East Anglia). The PTR-MS concentrations were averaged over 1s with an estimated precision of ± 37
184 ppt (Palmer, 2013).

185 Aerosol composition measurements used here were taken by i) refractory black carbon (BC)

186 mass and number measurements from a Single Particle Soot Photometer (SP2) (accuracy 20%,
187 precision 5%, 5s averaging time) and ii) non-refractory organic aerosol (OA) via an aerosol mass
188 spectrometer (precision $\sim 15\text{-}150\text{ ng m}^{-3}$) both operated by the University of Manchester (Jolleys et al.,
189 2014; Taylor et al., 2014). The number concentrations of the combined aerosol particles was measured
190 by Scanning Mobility Particle Sizer (SMPS) with 26 lognormally-spaced diameter bins ranging from
191 20-330 nm and corrected to STP. A full scan takes 60s (Palmer, 2013). The SMPS data was inverted
192 using the commonly-used Wiedensohler (1988) parameterisation, however recent work has suggested
193 that this may be quantitatively unreliable ~~in this situation for applications to aircraft data~~ due to
194 variations in the charging efficiency with pressure (López-Yglesias and Flagan, 2013; Leppä et al.,
195 2014). While this may have affected the magnitude of the number concentrations, no altitude
196 dependency was noted ~~in~~ the sizing data, so the conclusions of this paper regarding particle size are
197 unaffected.

198 The combination of gas and particle tracer measurements listed above were used to identify
199 flight periods of biomass-burning plume sampling, determine if SOA formation or OA evaporation may
200 have occurred in the plume, and characterize the size-distribution of aerosols within the plume.

201

202 **2.3 Plume Criteria**

203 We determine if measurements are in-plume versus out-of-plume using threshold plume criteria. We
204 designate sampling periods as in-plume if pre-specified threshold values of four tracer species: CO,
205 CH₃CN, BC, and OA, were exceeded. For out-of-plume conditions, we determine “background values”
206 for each tracer by averaging the tracers over the out-of-plume periods.

207 Carbon monoxide ($\tau_{\text{co}} \sim \text{months}$ (Staudt et al., 2001)) and acetonitrile ($\tau_{\text{ace}} \sim 6\text{ months}$
208 (Holzinger et al., 2005)) were used in conjunction as gaseous tracers due to their high mixing ratios in
209 biomass-burning plumes relative to the background and long atmospheric lifetimes relative to the
210 estimated plume transport times. The background CO levels were 80-120 ppbv with an overall average
211 of 100 ppbv. The threshold CO value was set to 150 ppbv (1.5 x [background]), with some CO
212 concentrations in-plume reaching ten times background concentrations (1000 ppbv). The threshold
213 CH₃CN level was 200 pptv (background $\sim 100\text{ pptv}$).

214 The particulate matter thresholds (BC number, OA mass) were introduced to ensure
215 high-enough aerosol contributions to the plume to analyze size-distributions. This ensured high-gas,
216 low-aerosol sampling periods were not included in the size-distribution analysis. At least one case of

217 this situation in BORTAS-B has been attributed by Franklin et al. (2014) to aerosol rainout during
218 transport. The mean background concentrations for both BC number and OA mass were minimal (< 20
219 cm^{-3} and $2 \mu\text{g m}^{-3}$ respectively). The threshold values were set to 50 cm^{-3} for BC number and $20 \mu\text{g m}^{-3}$
220 for OA mass. These thresholds for particles are higher relative to background than CO and CH₃CN
221 because we wanted to exclude a higher-elevation plume that had undergone aerosol wet deposition
222 (will be described later see Section 3.2).

223 The selected CO, CH₃CN, aerosol data, and flight altitude time series for Flight b622 is shown
224 in Figure 2. The flight is divided into transects (labeled 1-9 and colored) as seen in the altitude plot
225 (Figure 2, bottom). We use these in-plume time periods to differentiate between in-plume and
226 background aerosols throughout the paper.

227

228 **2.4 Model Description**

229 We use a Lagrangian box model to simulate the evolution of the biomass-burning size distribution due
230 to coagulation. The model has fifty-five logarithmically distributed size bins that correspond to the size
231 bins of the SMPS on the ARA and extend to both larger and smaller diameters. The model includes
232 coagulation and dilution as the only physical processes, with no chemistry or speciation of the aerosol
233 (we show in Section 3.2 that we cannot see evidence of net OA condensation/evaporation in the plume
234 over the sampling period). The model distributions are therefore limited by the lack of condensational
235 growth known to occur in BB plumes during the first few hours of aging (e.g. Reid et al. 1998).

236 _____ We use an inverse method to estimate the initial youngfresh (~ 1 hour) size-distributions by
237 successively running the model from emission initial conditions to BORTAS observation forward in
238 time and changing the initial size distribution until the model most closely matches the observed aged
239 size distribution. This method estimates the initial distribution assuming that coagulation was the only
240 physical processes affecting the in-plume particles. The box model does not include any cloud
241 interaction chemistry, which could have influenced the distribution considerably depending on
242 meteorological conditions, notably through wet deposition and aqueous chemistry.

243 Each model forward simulation requires the youngfresh size-distribution input as a single
244 lognormal mode with parameters: median diameter (D_{pm}), modal width (σ), and particle number (N_0).
245 For coagulation, we use the brownian coagulation kernel of Fuchs (1964). Dilution of the plume in
246 transport was modelled using a simple e-folding volume mixing time, τ_{dil} . This parameter controlled the
247 entrainment each timestep between the in-plume and background aerosol. The rate of plume dilution

248 may significantly affect the rate of coagulation throughout the simulation (the coagulation rate is
249 proportional to N^2). Different values of τ_{dil} were tested to account for a range of entrainment rates as the
250 dilution rate in the plume is relatively unconstrained. We test τ_{dil} values of 24, 36 and 48 hours. The 36
251 hr dilution timescale was ~~based on an estimate of~~ calculated as the mean timescale for dilution
252 from volume expansion from Gaussian plume equations with an initial plume width of 10 km in a
253 neutral stability environment (Klug, 1969): (note, however, that expansion occurs at faster timescales
254 early in the plume aging, and this timescale slows with time). The range (24 – 48 hrs) accounts for
255 atmospheric stability and plume width variations in the BORTAS source region. The model simulation
256 time is 48 hours based on the upper age limits shown in Table 1.

257 | To determine the best estimate for initial conditions, we simulate a range of youngfresh plume
258 parameters: median diameter, D_{pm} , modal width, σ , and number, N_0 . The input median diameter range
259 was between 60-120 nm (increment = 1 nm), with σ ranging from 1.0-2.5 (increment = 0.1) and N_0
260 ranging from 5,000- 150,000 cm^{-3} (increment = 500 cm^{-3}). The parameter space was optimized by
261 brute force (i.e. every combination of input parameters was simulations) for each set dilution time and
262 the final modelled size-distribution was compared to the observed in-plume size distribution by an
263 equally weighted objective function. The objective function used was the sum of the absolute residual
264 across the SMPS range. Modelled data outside of the SMPS size range was not used in the objective
265 function.

266

267 **3. Results**

268 **3.1 Observed size distributions**

269 Observed SMPS size-distributions for individual plume transects showed highly elevated particle
270 counts with little variation between transects and flights. The transect-divided data for Flight b622 are
271 shown in Figure 3. Transects 2-6 and 9, show a clearly elevated accumulation mode within the plume,
272 with a peak median diameters of 180-240 nm. Transects 1, 7 and 8 have significantly less data (< 3 data
273 points per size bin) due to the lesser in-plume sampling periods (incomplete SMPS scans).

274 Those transects with sufficient plume data (> 3 data points per bin) are plotted against their
275 accumulation mode median diameter D_{pm} in Figure 4. We do not observe any discernible trend in
276 size-distribution with the distance from the source fires in either median diameter or number
277 concentration. This lack of a trend suggests that the microphysical processing during the range of
278 distances sampled has smaller effects on the size distribution than the variability between plumes for

279 Flight b622. Similarly small inter-transect variation was seen for Flight b623 (not shown). The median
280 size-distributions show no bias based on altitude or ascent/descent rate as an artefact of SMPS flow rate
281 fluctuations from altitude changes (not shown).

282 The composite median distribution across all plume sampling periods and both flights is shown
283 in Figure 5a. This characteristic size distribution is presented as a median value, minimizing the
284 contributions of outlying data. Figure 5b shows the same composite distribution normalized by CO
285 concentration to attempt to account for differences in the amount of emissions from the source. The
286 plume particle size-distribution shows the median size distribution highlighted in black, with the 25th
287 and 75th percentiles outlined in red. A clearly defined accumulation mode was identified centred at D_{pm}
288 = 230 nm and with a modal width of 1.5, based on a single lognormal mode fit. Normalizing the plume
289 distribution by CO mixing ratio produced a very similar pattern shown in Figure 5b (accumulation
290 mode: $D_{pm} = 230$ nm, $\sigma = 1.4$). The composite background aerosol size-distribution (sampling periods
291 that failed the in-plume criteria) are seen in black (with 25th and 75th percentiles shown in gray) in
292 Figure 5a. It shows relatively constant $dN/d\log D_p$ concentrations across the SMPS range and is lacking
293 the concentrated accumulation mode found in-plume.

294 The aged composite size-distribution and associated lognormal parameters are similar to those
295 found in other field studies of aged biomass-burning emissions. Aged biomass-burning size
296 distributions compiled by Janhäll et al. (2010) for all different fuel types show a similar D_{pm} to modal
297 width ratio ($D_{pm} = 175 - 300$ nm, $\sigma = 1.7 - 1.3$). Capes et al. (2008) show a similar aged BB size
298 distribution [parametersmedian diameter](#) over West Africa during the DABEX campaign ($D_{pm} = 240$
299 nm). The ARCTAS-B campaign over Northern Canada sampled similar Boreal pyrogenic outflow and
300 collected very similar aged distributions of BC and OC constituents ($D_{pm} = 224 \pm 14$ nm, $\sigma = 1.33 \pm$
301 0.05) (Kondo et al., 2011).

302 Of note in the BORTAS-B plume size distribution is the elevated number concentrations of
303 small diameter particles (20-90 nm), which form an elevated small-diameter 'tail' of the distribution.
304 These higher concentrations were not expected due to the high rate of removal of small particles by
305 coagulation with the larger particles in the accumulation mode. We calculated first-order
306 coagulation-loss timescales to investigate the timescale of the removal of these small particles by the
307 larger plume particles. If these small particles were brought into the plume by entrainment of
308 background air, there would be an associated amount of time before these particles were lost by
309 coagulation. For the calculation, we assume brownian coagulation of entrained background aerosol

310 (bin range 20-90 nm) with the observed in-plume SMPS data (90-333 nm) and with artificial
311 large-diameter bins from 330 nm – 1 μ m (6 bins). These artificial bin concentrations were based on the
312 accumulation mode lognormal fit and account for those particle concentrations at sizes larger than
313 those measured by the SMPS but that nonetheless contribute to the coagulation scavenging of the
314 small-diameter particles. Particles with diameters $> 1 \mu\text{m}$ were ignored since their relative scarcity
315 relative to the large number of accumulation-mode particles causes a negligible impact on the
316 number-concentration driven coagulation process.

317 The predicted concentrations of background aerosol remaining after 24, 36 and 48 hours are
318 shown in Figure 6a. These times are within the estimated physical transport age ranges of the transects.
319 After 12 hours, coagulation alone has already caused a significant decrease in the concentrations of the
320 smallest measured particles, reducing them to levels well below the concentrations observed in plume
321 (red line). This deficit increases with time ($t=36$ hrs, $t=48$ hrs). The coagulation lifetimes of the
322 particles in this diameter range (30-90 nm) are seen in Figure 6b and extend into the tens of hours. Note
323 that the concentrations of these small-diameter particles are similar in the plume compared to the
324 background. This means that the entrainment rate of background air into the plume would need to be
325 much faster than the coagulation loss timescales (~ 5 hours for 20 nm particles) in order for
326 entrainment to sustain the number of small particles. If entrainment timescales were significantly
327 shorter than 5 hours, the plume would almost completely disperse into the background within 1 day.

328 There are a number of mechanisms other than entrainment that could explain the higher tail
329 concentrations found in plume despite the short coagulation lifetimes. In-plume nucleation and
330 subsequent growth to SMPS-detectable sizes could also partially account for sustained elevated small
331 particle concentrations. Hennigan et al. (2012) showed with the FLAME-III chamber studies that
332 in-plume nucleation was possible as a result of photochemical aging and SOA production in smoke
333 plumes. Nucleation modes in association with smoke plumes have also been observed previously in
334 field studies (Hobbs et al., 2003; Rissler et al., 2006). We attempted to determine the nucleation and
335 growth rates required to sustain the observed concentration of small particles; however, the necessary
336 condensational growth rates that were required to fit the observed data were unrealistically high, which
337 we see as evidence against nucleation/growth being the primary source of the small particles. Thus, we
338 are unsure of the source of these particles.

339

340 **3.2 Net production/loss of organic aerosol with time**

341 Enhancement ratios are a way of characterizing plume chemistry as a ratio of a specific species to a
342 reference species. This was done for the sampled BORTAS pyrogenic outflow by taking the excess
343 (background concentration removed) of the AMS organic aerosol normalized to the excess CO ($\Delta\text{OA}/$
344 ΔCO). Only those data which were in excess of the mean background ($\text{CO} = 100 \text{ ppbv}$, $\text{OA} = 2 \mu\text{g m}^{-3}$)
345 were compiled. The characteristic $\Delta\text{OA}/\Delta\text{CO}$ ratio can be used as a comparison value between fires of
346 different fuel type, phases or photochemical ages.

347 Since CO has a sufficiently long lifetime and is co-emitted with OA in abundance at the source,
348 any changes in the organic aerosol enhancement ratio over the lifetime of the plume are attributed to
349 in-plume chemistry. Entrainment of background air into the most concentrated sections of the plumes is
350 slow (timescale > 10 hours) and we consider any change in $\Delta\text{OA}/\Delta\text{CO}$ ratios to be attributable to
351 in-plume processes only. The formation of secondary organic aerosol is possible within the plume by
352 oxidation of organic vapors to lower-volatility products. Evaporation of less-volatile POA during
353 plume dilution competes with the SOA condensation. The net OA production is therefore: $\Delta\text{OA}_{\text{net}} =$
354 $\text{SOA}_{\text{prod}} - \text{OA}_{\text{evap}}$. Changes in the $\Delta\text{OA}/\Delta\text{CO}$ ratio over time can therefore indicate which of the two
355 processes is dominant.

356 The organic aerosol enhancement ratios for Flight b622 are shown in Figure 7. There is a fairly
357 pronounced altitude dependence as seen in Figure 7a, with several high altitude ($\sim 7 \text{ km}$) samples
358 having fairly low excess organic aerosol, but significant ΔCO (300 ppbv). This trend is featured in
359 Franklin et al. (2014) where the high-altitude plume showed evidence of an aerosol rainout event
360 causing low $\Delta\text{OA}/\Delta\text{CO}$ within the plume transected at those high altitudes.

361 We will focus on the lower-altitude plume where the aerosol was not rained out, so we employ a
362 height cutoff of 4.6 km to restrict the enhancement ratio calculations to lower-altitude, OA-rich plumes
363 least likely to have seen significant reduction in organic aerosol from wet deposition. The mean
364 enhancement ratios by transect are seen in Figure 7b (for transect locations see Figure 1). Only those
365 sampling periods that passed the OA and CO plume criteria (detailed above) are shown. The
366 lower-altitude plume enhancement ratio show correlations of $R^2 > 0.5$ for each transect with the
367 exception of Transect 8 ($R^2 = 0.26$).

368 Figure 8 shows $\Delta\text{OA}/\Delta\text{CO}$ as a function of the distance from the source fires (horizontal error
369 bars correspond to error due to the radius of the Ontario fire region, vertical error bars are calculated
370 from transect data scatter). Compared across transects, the enhancement ratios show no significant
371 trend (to P-value = 0.55). The average enhancement ratio is $0.143 \pm 0.01 [\mu\text{g m}^{-3} \text{ ppbv}^{-1}]$ and can be

372 considered characteristic of the aged boreal plume during these BORTAS flights.

373 The lack of trend in Figure 8 suggests that we cannot determine if there was any net
374 production/evaporation of OA happening inside the plume over this sampling period (plume ages: 1-2
375 days). Any SOA produced photochemically inside the plume is either being accompanied by an
376 opposing loss of POA or at such a rate that is below the observational variability over the sampled time
377 period. The statistically invariant $\Delta\text{OA}/\Delta\text{CO}$ does not discount evaporation-condensational cycling of
378 POA and SOA, or the effects such recondensation would have on the size-distribution (although there
379 was no apparent trend in the size distribution either [Figure 4]). No increase in normalized excess OA
380 fraction means significant levels of excess SOA were not likely driving condensational growth,
381 ensuring that coagulation was dominating the size-distribution evolution during the period of aging
382 between 1 day and 2 days since emission.

383
384 _____ Since no significant trend was found in size-distribution D_{pm} with distance from the source in
385 the observations (> 1000 km; see Figure 4), any effect of POA-SOA cycling on the shape of the
386 distribution cannot be isolated above the noise. However, it does not preclude that there was significant
387 net OA production/evaporation that occurred prior to or after this observed period as has been observed
388 in other BB field studies (e.g. Akagi et al. (2012); Yokelson et al. 2009).—Thus, although evidence of
389 photo-oxidation and chemical processing was observed in-plume by Parrington et al. (2013), any
390 chemical composition impact on the size-distribution at the ages observed here seems negligible.

391

392 **3.2 Estimation of the youngfresh biomass burning size distribution**

393 In this section, we test the parameter space of our microphysical model to estimate the youngfresh
394 (aged ~1-3 hr) plume size-distribution emitted from the source fires. We allowed the youngfresh
395 biomass-burning size distribution to evolve for 48 hours and compared the result to the observed SMPS
396 plume composite distribution to isolate the optimal youngfresh plume size-distribution parameters.
397 These were then compared to observed youngfresh BB size distributions for context.

398 The Lagrangian microphysical model was run for 48 hours with fixed entrainment coefficients
399 of $\tau_{\text{dil}}=24$ hrs, $\tau_{\text{dil}} = 36$ hours and $\tau_{\text{dil}}=48$ hours. Figure 9a shows the optimal youngfresh plume
400 distribution parameters that were obtained for each tested entrainment rate (with particle number
401 concentration per co-emitted CO above background). Figure 9b shows the modelled aged distributions
402 plotted with the measured distribution. None of the model runs can capture the elevated concentrations

403 in the tail particles in the SMPS data, though this is expected due to the coagulation-dominant aging in
404 the model (discussed above) and adds further uncertainty to the existence of this small tail.

405 The youngfresh plume size-distributions are unimodal with median diameters of 94 nm, 67 nm,
406 and 59 nm for $\tau_{dil}=24$ hrs, $\tau_{dil}=36$ hrs and $\tau_{dil}=48$ hrs, respectively ($\sigma = 1.7, 2.1, 2.8$, respectively). The
407 higher entrainment rate of background aerosol requires the youngfresh plume distribution to be
408 narrower (lower σ) and have an initial median diameter closer to the final diameter ($D_{pfinal} = 230$ nm).
409 The initial number concentrations in the youngfresh plume were found to be optimized at 62,500,
410 80,000, and 115,000 [cm^{-3}] for $\tau_{dil}=48$ hrs, $\tau_{dil}=36$ hrs and $\tau_{dil}=24$ hrs, respectively. The initial higher
411 concentrations, narrower modal width and larger median diameter are required for the higher
412 entrainment rates to account for the more rapid plume dilution and subsequently the slowing of the
413 coagulation rates. Normalized to estimated freshly emitted excess CO, the young plume number
414 concentrations are 37, 53, and 60 cm^{-3} ppbv $^{-1}$ (for $\tau_{dil}=24$ hrs, $\tau_{dil}=36$ hrs and $\tau_{dil}=48$ hrs respectively; see
415 Figure 9a). The similar magnitudes of these normalized size-distributions indicate a relatively robust
416 particle/CO ratio regardless of the dilution parameter, though in the absence of the source fire fuel
417 densities, a direct comparison to emission factors (kg^{-1}) cannot be made.–

418 As the exact aging time and dilution profiles are unknown in addition to uncertainties in the
419 plume age, we cannot say with certainty which of these estimates is best; however, these results
420 compare to the field observations presented in Janhäll et al. (2010) for fresh plume smoke (range: $D_{pm} =$
421 100-150 nm) and to small-scale lab experiments measuring fresh smoke (range: $D_{pm} = 30$ -90 nm)
422 (Hosseini et al., 2010). Capes et al. (2008) conducted a similar fresh-plume size-distribution
423 estimate from their observed DABEX aged African smoke data using a coagulation box-model without
424 dilution. Their estimates for very fresh smoke have a much smaller D_{pm} (~ 30 nm).

425 The freshf plume size distributions modelled here are very sensitive to microphysical processes
426 directly after emission. Very close to the source, rapid dilution and condensation (due to cooling) may
427 occur, which are not captured by the coagulation/dilution model we have developed. Thus the
428 modelled plumes are better categorized as 'young' rather than freshly emitted. The youngfresh-plume
429 distributions modelled in this study neglect any immediate effects of condensation and/or evaporation
430 of OA on the size-distribution during cooling and dilution respectively, and focus on the effects of
431 coagulation which shape the size-distribution over a longer timescale (~ 10 hrs). There is therefore an
432 associated uncertainty in the young distributions due to the exclusion of condensational growth from
433 the model, despite evidence of its effects on BB particle sizes especially during the first hours of aging

434 | [\(e.g. Reid et al. 1998\).](#)

435 Figure 10 shows a time series of the optimal modelled size distribution for $\tau_{\text{dil}} = 36$ hrs over the
436 48 hr period. The median diameter growth (black line) occurs more rapidly during the early stages of
437 the plume due to the higher particle concentrations before significant dilution. Eighty percent of the
438 final median diameter is achieved within 10 hrs of coagulation processing. [Less drastic but similar](#)
439 [rapid growth by coagulation was seen by Capes et al. \(2008\) in their coagulation box model. This quick](#)
440 [size distribution evolution within the early plume stages suggests that large grid box models \(global,](#)
441 [regional\) should be using aged biomass-burning size-distributions as input. Figure 10 also shows the](#)
442 [size-distribution growth slowing considerably as the particle concentrations decrease and perhaps can](#)
443 [provide an explanation for the lack of strong trend in the observed BORTAS \$D_{\text{pm}}\$ across transects](#)
444 [\(Figure 4\), which were already aged between 1-2 days when they were sampled. Less drastic but](#)
445 [similar rapid growth by coagulation was seen by Capes et al. \(2008\) in their coagulation box model.](#)
446 [This quick size distribution evolution within the early plume stages suggests that large grid box models](#)
447 [\(global, regional\) should be using aged biomass-burning size-distributions as input.](#)

448

449 **4. Conclusions**

450 The BORTAS-B campaign provided the opportunity to collect numerous gaseous and aerosol
451 measurements from aged North-American biomass-burning plumes in July, 2011. The boreal fire
452 emissions in northwestern Ontario were transported (1-2 days) downwind to where they were sampled
453 by the FAAM BAE-146 research aircraft. We analyzed the plume data from two research flights (b622
454 and b623) and found little variation in size-distributions between transects.

455 A characteristic size-distribution consistent between flights and transects was dominated by the
456 accumulation mode with $D_{\text{pm}} = 230$ nm and with $\sigma = 1.5$. This unimodal result is consistent with aged
457 biomass-burning observations found globally in the previous field studies [\(Capes et al., 2008; Janhäll et](#)
458 [al., 2010; Kondo et al., 2011\).](#)

459 We also found elevated concentrations of small-diameter particles in the plume contrary to their
460 coagulation lifetimes associated with the biomass-burning-associated accumulation mode. We were not
461 able to explain such concentrations by entrainment of background aerosol alone. The presence of such
462 concentrations in the size-distribution tail remains inconclusive.

463 The $\Delta\text{OA}/\Delta\text{CO}$ enhancement ratios across Flight b622 show a strong linear correlation below
464 4.6 km ($R^2 > 0.50$) with values between $(0.095 - 0.178) \pm 0.01 \mu\text{g m}^{-3} \text{ppbv}^{-1}$. We found no trend in

465 transect enhancement ratios with distance from the source, indicating no significant net SOA
466 production in-plume over the sampling period, though this does not preclude OA production or loss
467 during earlier stages of aging.

468 We used a microphysical model to estimate the youngfresh plume size distribution associated
469 with the BORTAS-B observations. Optimizing lognormal parameters for different assumed dilution
470 coefficients ($\tau_{dil} = 24, 36, 48$ hrs), the youngfresh plume size distribution had $D_{pm} = 59\text{-}94$ nm, $\sigma =$
471 $2.8\text{-}1.7$, and $N_0 = 62,500 - 115,000$ cm⁻³. (37 – 60 cm⁻³ ppbv⁻¹ normalized by initial co-emitted excess
472 CO). Though the model lacks condensation and chemical considerations, processing through
473 coagulation and dilution alone led to 80% of the observed 48-hour median-diameter growth within the
474 first 10 hrs. This suggests that global climate models should be using coagulation-aged BB size
475 distribution inputs to account for the rapid evolution in plume particle size occurring on scales smaller
476 than the gridbox length.

477

478 5. References

479

480 Adler, G., Flores, J. M., Abo Riziq, a., Borrmann, S. and Rudich, Y.: Chemical, physical, and optical
481 evolution of biomass burning aerosols: a case study, Atmos. Chem. Phys., 11(4), 1491–1503,
482 doi:10.5194/acp-11-1491-2011, 2011.

483 Akagi, S. K., Craven, J. S., Taylor, J. W., McMeeking, G. R., Yokelson, R. J., Burling, I. R., Urbanski,
484 S.P., Wold, C. E., Seinfeld, J. H., Coe, H., Alvarado, M. J. and Weise, D. R.: Evolution of trace
485 gases and particles emitted by a chaparral fire in California, Atmos. Chem. Phys., 12(3),
486 1397–1421, doi:10.5194/acp-12-1397-2012, 2012

487 Alonso-Blanco, E.: Impact of Biomass Burning on Aerosol Size Distribution, Aerosol Optical
488 Properties and Associated Radiative Forcing, Aerosol Air Qual. Res., 006, 708–724,
489 doi:10.4209/aaqr.2013.05.0163, 2014.

490 Andreae, M. O. and Merlet, P.: Emission of trace gases and aerosols from biomass burning, Global
491 Biogeochem. Cycles, 15(4), 955–966, doi:10.1029/2000GB001382, 2001.

492 Andreae, M. O., Artaxo, P., Fischer, H., Freitas, S. R., Grégoire, J.-M., Hansel, A., Hoor, P., Kormann,
493 R., Krejci, R., Lange, L., Lelieveld, J., Lindinger, W., Longo, K., Peters, W., de Reus, M.,
494 Scheeren, B., Silva Dias, M. A. F., Ström, J., van Velthoven, P. F. J. and Williams, J.: Transport of
495 biomass burning smoke to the upper troposphere by deep convection in the equatorial region,
496 Geophys. Res. Lett., 28(6), 951–954, doi:10.1029/2000GL012391, 2001.

497 Bauer, S. E., Menon, S., Koch, D., Bond, T. C. and Tsigaridis, K.: A global modeling study on
498 carbonaceous aerosol microphysical characteristics and radiative effects, Atmos. Chem. Phys.,
499 10(15), 7439–7456, doi:10.5194/acp-10-7439-2010, 2010.

500 Capes, G., Johnson, B., McFiggans, G., Williams, P. I., Haywood, J. and Coe, H.: Aging of biomass

501 burning aerosols over West Africa: Aircraft measurements of chemical composition, microphysical
502 properties, and emission ratios, *J. Geophys. Res.*, 113, D00C15, doi:10.1029/2008JD009845,
503 2008.

504 Carrico, C. M., Petters, M. D., Kreidenweis, S. M., Sullivan, A. P., McMeeking, G. R., Levin, E. J. T.,
505 Engling, G., Malm, W. C. and Collett, J. L.: Water uptake and chemical composition of fresh
506 aerosols generated in open burning of biomass, *Atmos. Chem. Phys.*, 10(11), 5165–5178,
507 doi:10.5194/acp-10-5165-2010, 2010.

508 Chen, W.T., Lee, Y. H., Adams, P. J., Nenes, A. and Seinfeld, J. H.: Will black carbon mitigation
509 dampen aerosol indirect forcing?, *Geophys. Res. Lett.*, 37(9), L09801,
510 doi:10.1029/2010GL042886, 2010.

511 Cubison, M. J., Ortega, A. M., Hayes, P. L., Farmer, D. K., Day, D., Lechner, M. J., Brune, W. H., Apel,
512 E., Diskin, G. S., Fisher, J. A., Fuelberg, H. E., Hecobian, A., Knapp, D. J., Mikoviny, T., Riemer,
513 D., Sachse, G. W., Sessions, W., Weber, R. J., Weinheimer, A. J., Wisthaler, A. and Jimenez, J. L.:
514 Effects of aging on organic aerosol from open biomass burning smoke in aircraft and laboratory
515 studies, *Atmos. Chem. Phys.*, 11(23), 12049–12064, doi:10.5194/acp-11-12049-2011, 2011.

516 DeCarlo, P. F., Ulbrich, I. M., Crouse, J., de Foy, B., Dunlea, E. J., Aiken, A. C., Knapp, D.,
517 Weinheimer, A. J., Campos, T., Wennberg, P. O. and Jimenez, J. L.: Investigation of the sources
518 and processing of organic aerosol over the Central Mexican Plateau from aircraft measurements
519 during MILAGRO, *Atmos. Chem. Phys.*, 10(12), 5257–5280, doi:10.5194/acp-10-5257-2010,
520 2010.

521 [Engelhart, G. J., Hennigan, C. J., Miracolo, M. A., Robinson, A. L. and Pandis, S. N.: Cloud](#)
522 [condensation nuclei activity of fresh primary and aged biomass burning aerosol, *Atmos. Chem.*](#)
523 [Phys., 12\(15\), 7285–7293, doi:10.5194/acp-12-7285-2012, 2012.](#)

524 Franklin, J. E., Drummond, J. R., Griffin, D., Pierce, J. R., Waugh, D. L., Palmer, P. I., Parrington, M.,
525 Lee, J. D., Lewis, A. C., Rickard, A. R., Taylor, J. W., Allan, J. D., Coe, H., Walker, K. A.,
526 Chisholm, L., Duck, T. J., Hopper, J. T., Blanchard, Y., Gibson, M. D., Curry, K. R., Sakamoto, K.
527 M., Lesins, G., Dan, L., Kliever, J. and Saha, A.: A case study of aerosol scavenging in a biomass
528 burning plume over eastern Canada during the 2011 BORTAS field experiment, *Atmos. Chem.*
529 *Phys.*, 14(16), 8449–8460, doi:10.5194/acp-14-8449-2014, 2014.

530 Fuchs, N. A.: *The Mechanics of Aerosols*, Oxford: Pergamon Press., 1964.

531 Grieshop, A. P., Logue, J. M., Donahue, N. M. and Robinson, A. L.: Laboratory investigation of
532 photochemical oxidation of organic aerosol from wood fires 1: measurement and simulation of
533 organic aerosol evolution, *Atmos. Chem. Phys.*, 9(4), 1263–1277, doi:10.5194/acp-9-1263-2009,
534 2009.

535 Haywood, J. and Boucher, O.: Estimates of the direct and indirect radiative forcing due to tropospheric
536 aerosols: a review, *Rev. Geophys.*, 38, 513–543, doi:10.1029/1999RG000078, 2000.

537 Hecobian, A., Liu, Z., Hennigan, C. J., Huey, L. G., Jimenez, J. L., Cubison, M. J., Vay, S., Diskin, G.
538 S., Sachse, G. W., Wisthaler, A., Mikoviny, T., Weinheimer, A. J., Liao, J., Knapp, D. J.,
539 Wennberg, P. O., Kürten, A., Crouse, J. D., Clair, J. St., Wang, Y. and Weber, R. J.: Comparison
540 of chemical characteristics of 495 biomass burning plumes intercepted by the NASA DC-8 aircraft
541 during the ARCTAS/CARB-2008 field campaign, *Atmos. Chem. Phys.*, 11(24), 13325–13337,
542 doi:10.5194/acp-11-13325-2011, 2011.

- 543 Hennigan, C. J., Miracolo, M. A., Engelhart, G. J., May, A. A., Presto, A. A., Lee, T., Sullivan, A. P.,
544 McMeeking, G. R., Coe, H., Wold, C. E., Hao, W.-M., Gilman, J. B., Kuster, W. C., de Gouw, J.,
545 Schichtel, B. A., Kreidenweis, S. M. and Robinson, A. L.: Chemical and physical transformations
546 of organic aerosol from the photo-oxidation of open biomass burning emissions in an
547 environmental chamber, *Atmos. Chem. Phys.*, 11(15), 7669–7686, doi:10.5194/acp-11-7669-2011,
548 2011.
- 549 Hennigan, C. J., Westervelt, D. M., Riipinen, I., Engelhart, G. J., Lee, T., Collett, J. L., Pandis, S. N.,
550 Adams, P. J. and Robinson, A. L.: New particle formation and growth in biomass burning plumes:
551 An important source of cloud condensation nuclei, *Geophys. Res. Lett.*, 39(9), n/a–n/a,
552 doi:10.1029/2012GL050930, 2012.
- 553 Heringa, M. F., DeCarlo, P. F., Chirico, R., Tritscher, T., Dommen, J., Weingartner, E., Richter, R.,
554 Wehrle, G., Prévôt, A. S. H. and Baltensperger, U.: Investigations of primary and secondary
555 particulate matter of different wood combustion appliances with a high-resolution time-of-flight
556 aerosol mass spectrometer, *Atmos. Chem. Phys.*, 11(12), 5945–5957,
557 doi:10.5194/acp-11-5945-2011, 2011.
- 558 Hobbs, P. V., Sinha, P., Yokelson, R. J., Christian, T. J., Blake, D. R., Gao, S., Kirchstetter, T. W.,
559 Novakov, T. and Pilewskie, P.: Evolution of gases and particles from a savanna fire in South
560 Africa, *J. Geophys. Res.*, 108(D13), doi:10.1029/2002JD002352, 2003.
- 561 Holzinger, R., Williams, J., Salisbury, G., Klüpfel, T., de Reus, M., Traub, M., Crutzen, P. J. and
562 Lelieveld, J.: Oxygenated compounds in aged biomass burning plumes over the Eastern
563 Mediterranean: evidence for strong secondary production of methanol and acetone, *Atmos. Chem.*
564 *Phys.*, 5(1), 39–46, doi:10.5194/acp-5-39-2005, 2005.
- 565 Hosseini, S., Li, Q., Cocker, D., Weise, D., Miller, A., Shrivastava, M., Miller, J. W., Mahalingam, S.,
566 Princevac, M. and Jung, H.: Particle size distributions from laboratory-scale biomass fires using
567 fast response instruments, *Atmos. Chem. Phys.*, 10(16), 8065–8076,
568 doi:10.5194/acp-10-8065-2010, 2010.
- 569 Hudson, P. K., Murphy, D. M., Cziczo, D. J., Thomson, D. S., de Gouw, J. A., Warneke, C., Holloway,
570 J., Jost, H.-J. and Hübler, G.: Biomass-burning particle measurements: Characteristic composition
571 and chemical processing, *J. Geophys. Res.*, 109(D23), D23S27, doi:10.1029/2003JD004398,
572 2004.
- 573 [Huffman, J. A., Docherty, K. S., Mohr, C., Cubison, M. J., Ulbrich, I. M., Ziemann, P. J., Onasch, T. B.](#)
574 [and Jimenez, J. L.: Chemically-Resolved Volatility Measurements of Organic Aerosol from](#)
575 [Different Sources, *Environ. Sci. Technol.*, 43\(14\), 5351–5357, doi:10.1021/es803539d, 2009.](#)
- 576 Jacobson, M. Z.: Strong radiative heating due to the mixing state of black carbon in atmospheric
577 aerosols, *Nature*, 409(6821), 695–697, 2001.
- 578 Janhäll, S., Andreae, M. O. and Pöschl, U.: Biomass burning aerosol emissions from vegetation fires :
579 particle number and mass emission factors and size distributions, *Atmos. Chem. Phys.*, 1427–1439,
580 2010.
- 581 Klug, W. : A method for determining diffusion conditions from synoptic observations, *Staub-Reinhalt.*
582 *Luft*, 29, 14–20, 1969.
583
- 584 Kondo, Y., Matsui, H., Moteki, N., Sahu, L., Takegawa, N., Kajino, M., Zhao, Y., Cubison, M. J.,

585 Jimenez, J. L., Vay, S., Diskin, G. S., Anderson, B., Wisthaler, A., Mikoviny, T., Fuelberg, H. E.,
586 Blake, D. R., Huey, G., Weinheimer, A. J., Knapp, D. J. and Brune, W. H.: Emissions of black
587 carbon, organic, and inorganic aerosols from biomass burning in North America and Asia in 2008,
588 *J. Geophys. Res.*, 116(D8), D08204, doi:10.1029/2010JD015152, 2011.

589 [Jolleys, M. D., Coe, H., McFiggans, G., Taylor, J. W., O'Shea, S. J., Le Breton, M., Bauguitte, S. J.-B.,](#)
590 [Moller, S., Di Carlo, P., Aruffo, E., Palmer, P. I. and Lee, J. D.: Properties and evolution of](#)
591 [biomass burning organic aerosol from Canadian boreal forest fires, *Atmos. Chem. Phys. Discuss.*,](#)
592 [14\(18\), 25095–25138, doi:10.5194/acpd-14-25095-2014, 2014.](#)

593 Lee, L. A., Pringle, K. J., Reddington, C. L., Mann, G. W., Stier, P., Spracklen, D. V., Pierce, J. R. and
594 Carslaw, K. S.: The magnitude and causes of uncertainty in global model simulations of cloud
595 condensation nuclei, *Atmos. Chem. Phys.*, 13(17), 8879–8914, doi:10.5194/acp-13-8879-2013,
596 2013.

597 Lee, S., Kim, H. K., Yan, B., Cobb, C. E., Hennigan, C., Nichols, S., Chamber, M., Edgerton, E. S.,
598 Jansen, J. J., Hu, Y., Zheng, M., Weber, R. J. and Russell, A. G.: Diagnosis of aged prescribed
599 burning plumes impacting an urban area., *Environ. Sci. Technol.*, 42(5), 1438–44, 2008.

600 Leppä, J., Mui, W., Grantz, A. M. and Flagan, R. C.: OP10-5, Importance of charger ion properties in
601 size distribution measurements, International Aerosol Conference, August 28 - September 2,
602 BEXCO, Busan, Korea, 2014.

603 Levin, E. J. T., McMeeking, G. R., Carrico, C. M., Mack, L. E., Kreidenweis, S. M., Wold, C. E.,
604 Moosmüller, H., Arnott, W. P., Hao, W. M., Collett, J. L. and Malm, W. C.: Biomass burning
605 smoke aerosol properties measured during Fire Laboratory at Missoula Experiments (FLAME), *J.*
606 *Geophys. Res.*, 115(D18), D18210, doi:10.1029/2009JD013601, 2010.

607 López-Yglesias, X., and Flagan, R. C.: Ion–Aerosol Flux Coefficients and the Steady-State Charge
608 Distribution of Aerosols in a Bipolar Ion Environment, *Aerosol Sci. Technol.*, 47, 688-704,
609 10.1080/02786826.2013.783684, 2013.

610 [May, A. A., Levin, E. J. T., Hennigan, C. J., Riipinen, I., Lee, T., Collett, J. L., Jimenez, J. L.,](#)
611 [Kreidenweis, S. M. and Robinson, A. L.: Gas-particle partitioning of primary organic aerosol](#)
612 [emissions: 3. Biomass burning, *J. Geophys. Res. Atmos.*, 118\(19\), 11,327–11,338,](#)
613 [doi:10.1002/jgrd.50828, 2013.](#)

614 McMeeking, G. R., Kreidenweis, S. M., Baker, S., Carrico, C. M., Chow, J. C., Collett, J. L., Hao, W.
615 M., Holden, A. S., Kirchstetter, T. W., Malm, W. C., Moosmüller, H., Sullivan, A. P. and Wold, C.
616 E.: Emissions of trace gases and aerosols during the open combustion of biomass in the laboratory,
617 *J. Geophys. Res.*, 114(D19), D19210, doi:10.1029/2009JD011836, 2009.

618 Myhre, G., D. Shindell, F.-M. Bréon, W. Collins, J. Fuglestedt, J. Huang, D. Koch, J.-F. Lamarque, D.
619 Lee, B. Mendoza, T. Nakajima, A. Robock, G. Stephens, T. Takemura and H. Zhang:
620 Anthropogenic and Natural Radiative Forcing. In: *Climate Change 2013: The Physical Science*
621 *Basis. Contribution of Working Group I to the Fifth Assessment Report of the Intergovernmental*
622 *Panel on Climate Change* [Stocker, T.F., D. Qin, G.-K. Plattner, M. Tignor, S.K. Allen, J.
623 Boschung, A. Nauels, Y. Xia, V. Bex and P.M. Midgley (eds.)]. Cambridge University Press,
624 Cambridge, United Kingdom and New York, NY, USA, 659-740, 2013.

625 Okoshi, R., Rasheed, A., Chen Reddy, G., McCrowey, C. J. and Curtis, D. B.: Size and mass
626 distributions of ground-level sub-micrometer biomass burning aerosol from small wildfires,

- 627 Atmos. Environ., 89, 392–402, doi:10.1016/j.atmosenv.2014.01.024, 2014.
- 628 Ontario Ministry of Natural Resources and Forestry. 2011 Forest Fire Summary.
629 <https://www.ontario.ca/law-and-safety/forest-fires>. Accessed June 18, 2012.
- 630 Ortega, A. M., Day, D. A., Cubison, M. J., Brune, W. H., Bon, D., de Gouw, J. A. and Jimenez, J. L.:
631 Secondary organic aerosol formation and primary organic aerosol oxidation from biomass-burning
632 smoke in a flow reactor during FLAME-3, Atmos. Chem. Phys., 13(22), 11551–11571,
633 doi:10.5194/acp-13-11551-2013, 2013.
- 634 Palmer, P. I., Parrington, M., Lee, J. D., Lewis, A. C., Rickard, A. R., Bernath, P. F., Duck, T. J., Waugh,
635 D. L., Tarasick, D. W., Andrews, S., Aruffo, E., Bailey, L. J., Barrett, E., Bauguitte, S. J.-B., Curry,
636 K. R., Di Carlo, P., Chisholm, L., Dan, L., Forster, G., Franklin, J. E., Gibson, M. D., Griffin, D.,
637 Helmig, D., Hopkins, J. R., Hopper, J. T., Jenkin, M. E., Kindred, D., Kliever, J., Le Breton, M.,
638 Matthiesen, S., Maurice, M., Moller, S., Moore, D. P., Oram, D. E., O'Shea, S. J., Owen, R. C.,
639 Pagniello, C. M. L. S., Pawson, S., Percival, C. J., Pierce, J. R., Punjabi, S., Purvis, R. M.,
640 Remedios, J. J., Rotermund, K. M., Sakamoto, K. M., da Silva, A. M., Strawbridge, K. B., Strong,
641 K., Taylor, J., Trigwell, R., Tereszchuk, K. A., Walker, K. A., Weaver, D., Whaley, C., and Young,
642 J. C.: Quantifying the impact of BOREal forest fires on Tropospheric oxidants over the Atlantic
643 using Aircraft and Satellites (BORTAS) experiment: design, execution and science overview,
644 Atmos. Chem. Phys., 13, 6239-6261, doi:10.5194/acp-13-6239-2013, 2013.
- 645 Parrington, M., Palmer, P. I., Lewis, A. C., Lee, J. D., Rickard, A. R., Di Carlo, P., Taylor, J. W.,
646 Hopkins, J. R., Punjabi, S., Oram, D. E., Forster, G., Aruffo, E., Moller, S. J., Bauguitte, S. J.-B.,
647 Allan, J. D., Coe, H. and Leigh, R. J.: Ozone photochemistry in boreal biomass burning
648 plumes Parrington, M., Palmer, P. I., Lewis, A. C., Lee, J. D., Rickard, A. R., Di Carlo, P., ...
649 Leigh, R. J. (2013). Ozone photochemistry in boreal biomass burning plumes. Atmospheric
650 Chemistry and Physics, 13, Atmos. Chem. Phys., 13(15), 7321–7341,
651 doi:10.5194/acp-13-7321-2013, 2013.
- 652 Parrish, D. D., Stohl, A., Forster, C., Atlas, E. L., Blake, D. R., Goldan, P. D., Kuster, W. C. and de
653 Gouw, J. A.: Effects of mixing on evolution of hydrocarbon ratios in the troposphere, J. Geophys.
654 Res., 112(D10), D10S34, doi:10.1029/2006JD007583, 2007.
- 655 Petters, M. D. and Kreidenweis, S. M.: A single parameter representation of hygroscopic growth and
656 cloud condensation nucleus activity, Atmos. Chem. Phys., 7(8), 1961–1971,
657 doi:10.5194/acp-7-1961-2007, 2007.
- 658 Petters, M. D., Carrico, C. M., Kreidenweis, S. M., Prenni, A. J., DeMott, P. J., Collett, J. L. and
659 Moosmüller, H.: Cloud condensation nucleation activity of biomass burning aerosol, J. Geophys.
660 Res., 114(D22), D22205, doi:10.1029/2009JD012353, 2009.
- 661 Pierce, J. R., Chen, K. and Adams, P. J.: Contribution of primary carbonaceous aerosol to cloud
662 condensation nuclei: processes and uncertainties evaluated with a global aerosol microphysics
663 model, Atmos. Chem. Phys., 7, 5447–5466, 2007.
- 664 Reddington, C. L., Carslaw, K. S., Spracklen, D. V., Frontoso, M. G., Collins, L., Merikanto, J.,
665 Minikin, A., Hamburger, T., Coe, H., Kulmala, M., Aalto, P., Flentje, H., Plass-Dülmer, C.,
666 Birmili, W., Wiedensohler, A., Wehner, B., Tuch, T., Sonntag, A., O'Dowd, C. D., Jennings, S. G.,
667 Dupuy, R., Baltensperger, U., Weingartner, E., Hansson, H.-C., Tunved, P., Laj, P., Sellegri, K.,
668 Boulon, J., Putaud, J.-P., Gruening, C., Swietlicki, E., Roldin, P., Henzing, J. S., Moerman, M.,
669 Mihalopoulos, N., Kouvarakis, G., Ždímal, V., Zíková, N., Marinoni, A., Bonasoni, P. and Duchi,

670 R.: Primary versus secondary contributions to particle number concentrations in the European
671 boundary layer, *Atmos. Chem. Phys.*, 11(23), 12007–12036, doi:10.5194/acp-11-12007-2011,
672 2011.

673 Reid, J. S., Hobbs, P. and Ferek, R.: Physical, chemical, and optical properties of regional hazes
674 dominated by smoke in Brazil, *J. Geophys. Res.*, 103(98), 32059–32080, DOI:
675 10.1029/98JD00458, 1998.

676 Reid, J. S., Hyer, E. J., Prins, E. M., Westphal, D. L., Zhang, J., Wang, J., Christopher, S. A., Curtis, C.
677 A., Schmidt, C. C., Eleuterio, D. P., Richardson, K. A. and Hoffman, J. P.: Global Monitoring and
678 Forecasting of Biomass-Burning Smoke: Description of and Lessons From the Fire Locating and
679 Modeling of Burning Emissions (FLAMBE) Program, *IEEE J. Sel. Top. Appl. Earth Obs. Remote
680 Sens.*, 2(3), 144–162, doi:10.1109/JSTARS.2009.2027443, 2009.

681 Reid, J. S., Koppmann, R., Eck, T. F. and Eleuterio, D. P.: A review of biomass burning emissions part
682 II: intensive physical properties of biomass burning particles, *Atmos. Chem. Phys.*, 5(3), 799–825,
683 doi:10.5194/acp-5-799-2005, 2005.

684 Rissler, J., Vestin, A., Swietlicki, E., Fisch, G., Zhou, J., Artaxo, P. and Andreae, M. O.: Size
685 distribution and hygroscopic properties of aerosol particles from dry-season biomass burning in
686 Amazonia, *Atmos. Chem. Phys.*, 6, 471–491, 2006.

687 Seinfeld, J. H. and Pandis, S. N.: *Atmospheric chemistry and physics: from air pollution to climate
688 change*, Hoboken, N. J., Wiley, 2006.

689 Spracklen, D. V., Carslaw, K. S., Pöschl, U., Rap, A. and Forster, P. M.: Global cloud condensation
690 nuclei influenced by carbonaceous combustion aerosol, *Atmos. Chem. Phys.*, 11(17), 9067–9087,
691 doi:10.5194/acp-11-9067-2011, 2011.

692 Staudt, A. C., Jacob, D. J., Logan, J. A. and Sachse, G. W.: Continental sources, transoceanic
693 transport, and interhemispheric exchange of carbon, *J. Geophys. Res.*, 106, 32571–32589, DOI:
694 10.1029/2001JD900078, 2001.

695 Taylor, J. W., Allan, J. D., Allen, G., Coe, H., Williams, P. I., Flynn, M. J., Le Breton, M., Muller, J. B.
696 A., Percival, C. J., Oram, D., Forster, G., Lee, J. D., Rickard, A. R. and Palmer, P. I.:
697 Size-dependent wet removal of black carbon in Canadian biomass burning plumes, *Atmos. Chem.
698 Phys. Discuss.*, 14(13), 19469–19513, doi:10.5194/acpd-14-19469-2014, 2014.

699 Van der Werf, G. R., Randerson, J. T., Giglio, L., Collatz, G. J., Mu, M., Kasibhatla, P. S., Morton, D.
700 C., DeFries, R. S., Jin, Y. and van Leeuwen, T. T.: Global fire emissions and the contribution of
701 deforestation, savanna, forest, agricultural, and peat fires (1997–2009), *Atmos. Chem. Phys.*,
702 10(23), 11707–11735, doi:10.5194/acp-10-11707-2010, 2010.

703 Wiedensohler, A.: An Approximation of the Bipolar Charge-Distribution for Particles in the
704 Sub-Micron Size Range, *J. Aerosol. Sci.*, 19, 387–389, 1988.

705 Wiedinmyer, C., Akagi, S. K., Yokelson, R. J., Emmons, L. K., Al-Saadi, J. A., Orlando, J. J. and Soja,
706 A. J.: The Fire INventory from NCAR (FINN): a high resolution global model to estimate the
707 emissions from open burning, *Geosci. Model Dev.*, 4(3), 625–641, doi:10.5194/gmd-4-625-2011,
708 2011.

709 Yokelson, R. J., Crounse, J. D., Decarlo, P. F., Karl, T., Urbanski, S., Atlas, E., Campos, T. and
710 Shinozuka, Y.: Emissions from biomass burning in the Yucatan, *Atmos. Chem. Phys.*, 5785–5812,

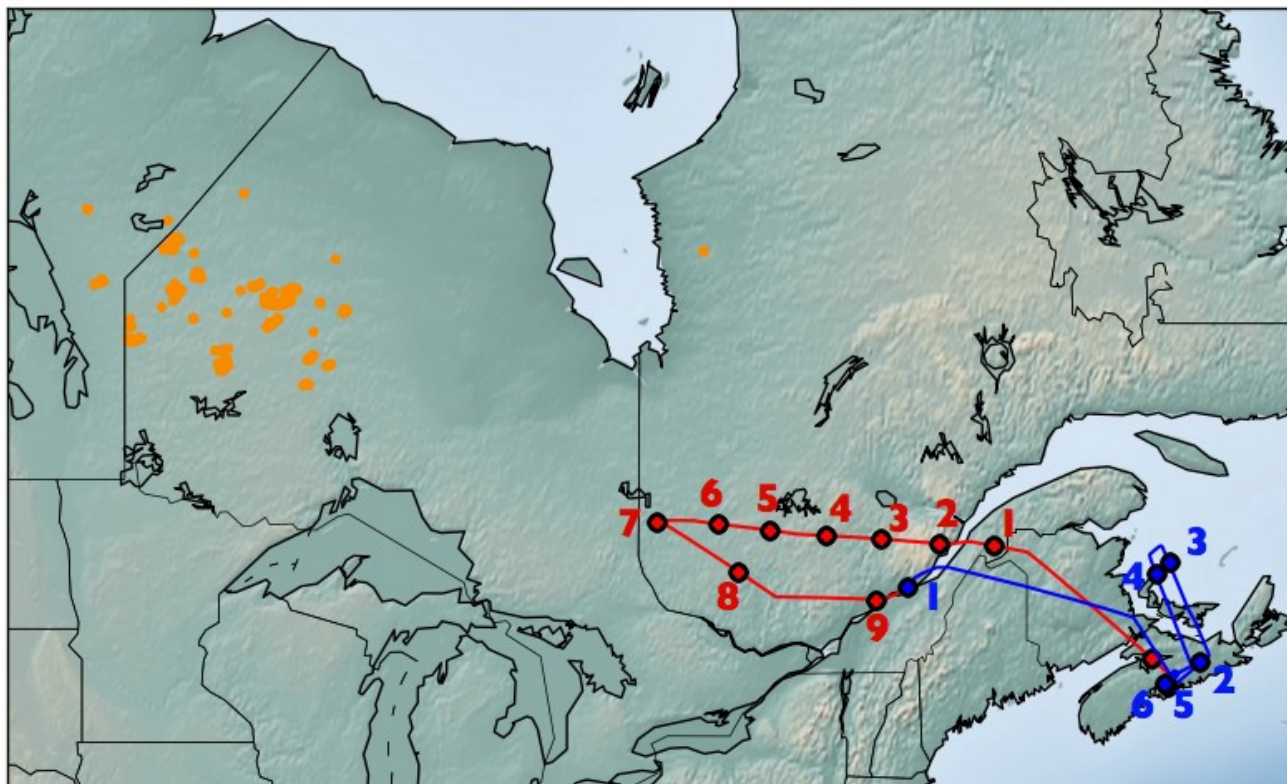
711 2009.

712

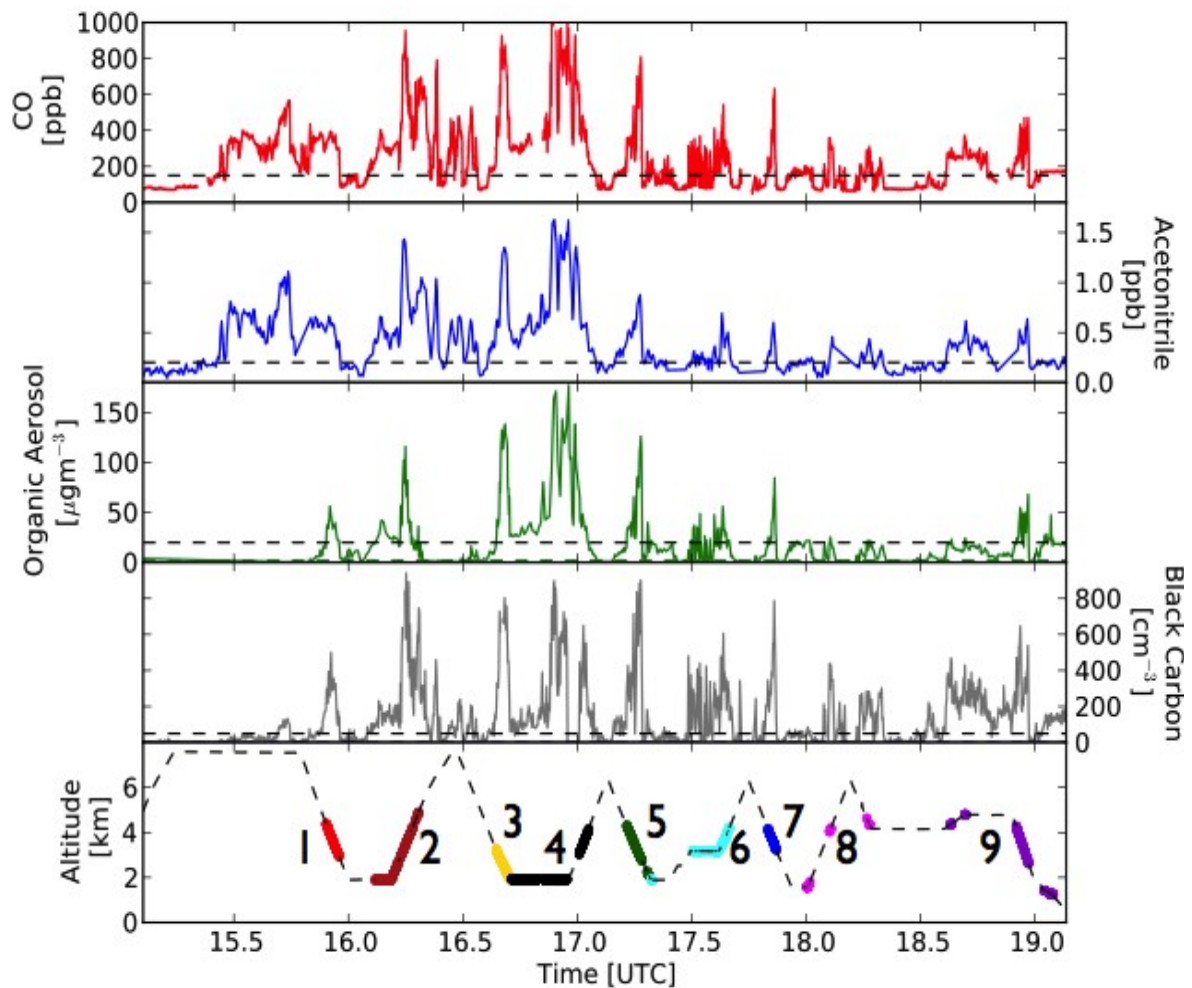
713 **Table 1.** Approximate physical transport age and distance of numbered flight transect midpoints from
 714 source fires. Ages were estimated by HYSPLIT back trajectories. The large ranges in the determined
 715 values are due to the large extent of the source fire region and variability in fire conditions. The
 716 distances are given from transect midpoints to the source fire region (± 150 km).
 717

Transect #	Approx. physical Age [hrs]	Approx. distance from source [km]
<i>Flight b622</i>		
1	27 - 32	1450 - 1750
2	27 - 32	1350 - 1650
3	27 - 32	1250 - 1550
4	27 - 32	1150 - 1450
5	18 - 25	1050 - 1350
6	18 - 25	850 - 1150
7	18 - 25	850 - 1150
8	18 - 25	1050 - 1350
9	24 - 30	1350 - 1650
<i>Flight b623</i>		
1	24 - 36	1350 - 1650
2	28 - 36	2050 - 2350
3 - 4	28 - 36	1850 - 2150
5 - 6	28 - 36	1950 - 2250

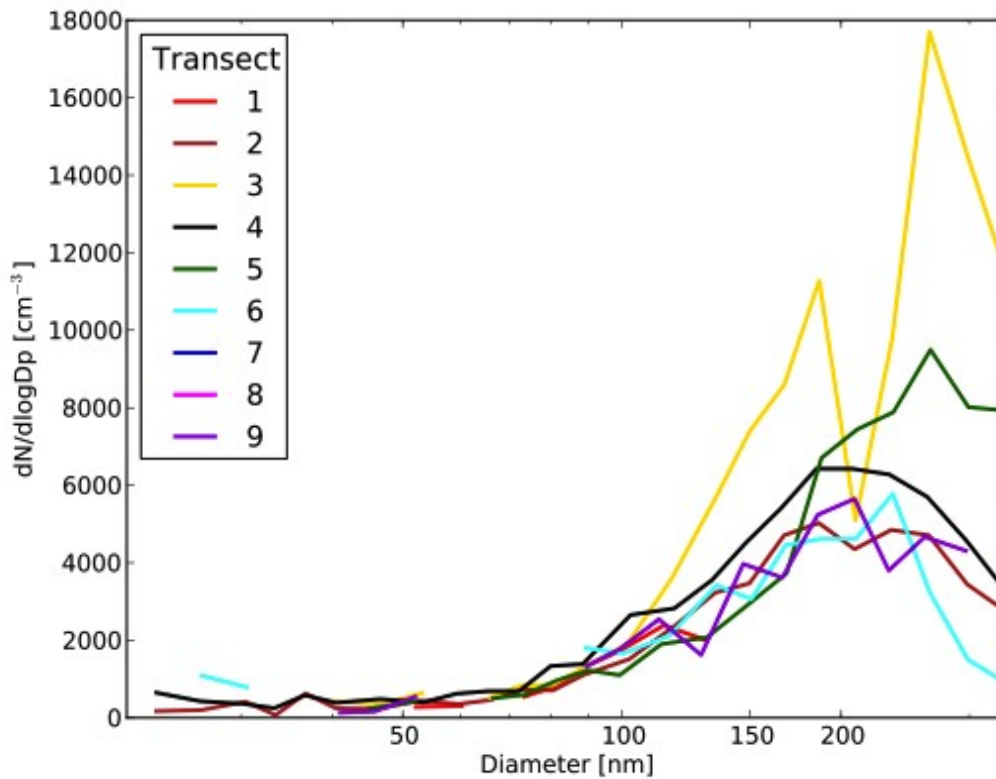
718



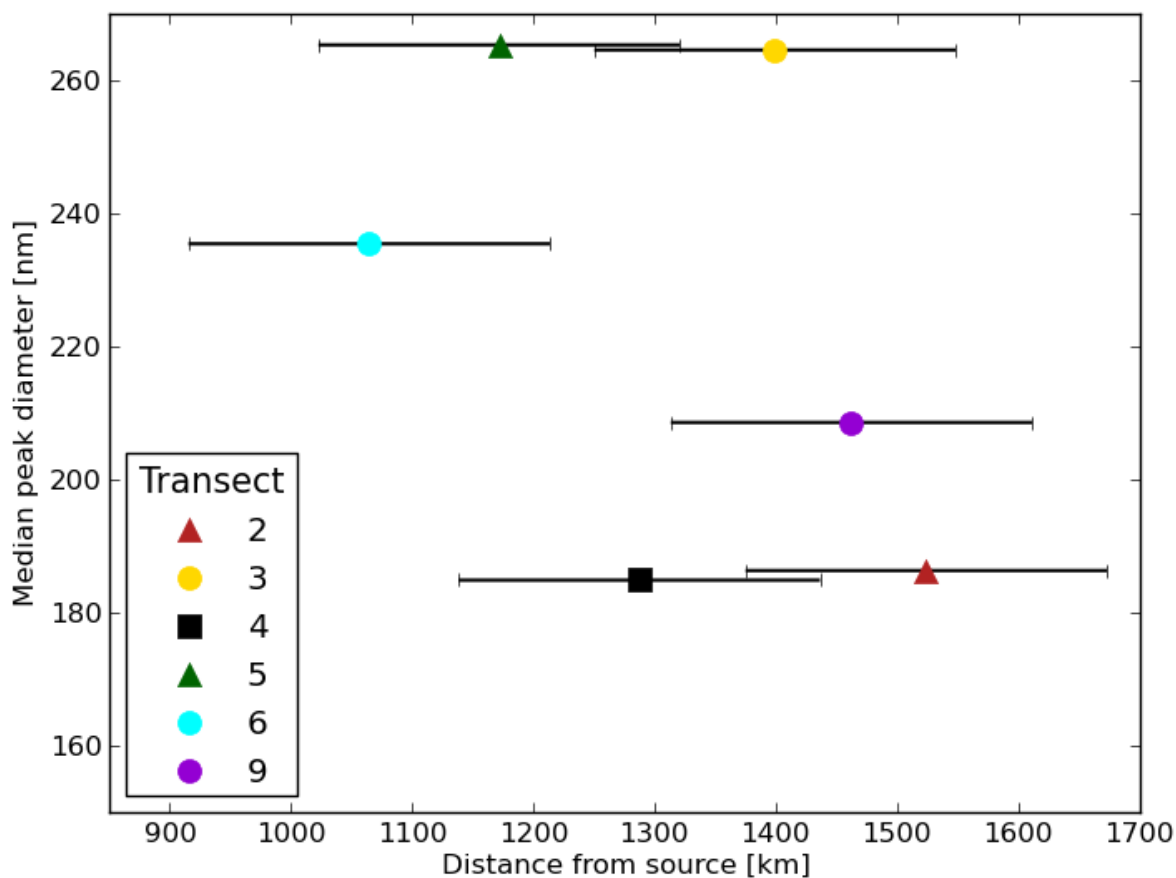
720 **Figure 1.** BORTAS-B ARA research flights b622 (red) from Nova Scotia to Quebec, and the return
721 flight b623 (blue) both on July 20-21, 2011. Circles represent midpoints of ascent/descent transects
722 along the flight paths. The ARA flew through biomass-burning emissions originating from fires in
723 Northwestern Ontario. The July 17-20, 2011 MODIS hotspot fires (fire radiative power >100 MW) are
724 plotted in orange.



726 **Figure 2.** Time series of BORTAS-B aircraft measurements of biomass-burning tracer species for
 727 Flight b622. Threshold values (dashed black lines) were used across four species as plume criteria: i)
 728 CO (red, threshold = 150 ppb), ii) Acetonitrile (blue, threshold = 200 pptv), iii) Organic aerosols
 729 (green, mass threshold= 20 $\mu\text{g m}^{-3}$, at STP), iv) Black carbon (grey, number threshold = 50 cm^{-3} , at
 730 STP). The bottom panel shows flight altitude with plume sampling periods coloured. The plume data is
 731 further divided into transects (1-9 in red-violet).

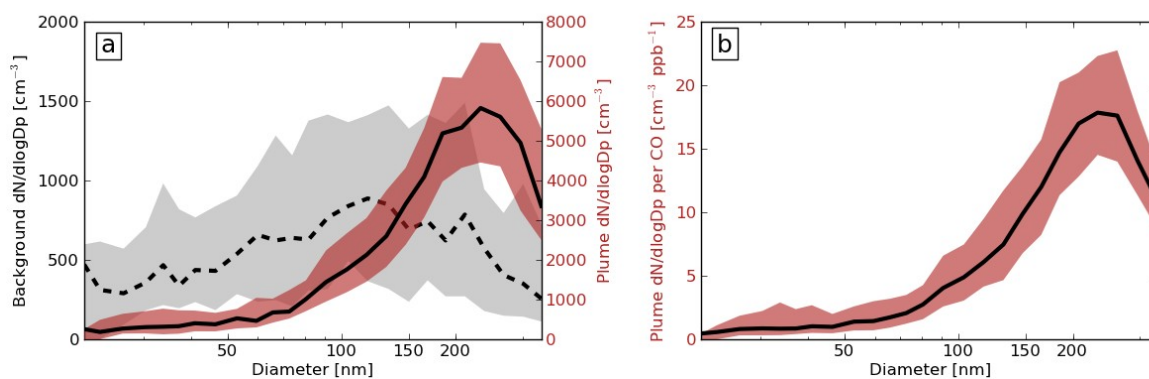


733 **Figure 3.** Median plume number size distributions (corrected to cm^{-3} at STP) divided by transect for
 734 Flight b622. All size distributions show a consistent accumulation mode with $D_{\text{pm}} \sim 220$ nm. Size bins
 735 with less than three data points in any transect are not shown, limiting the contributions from transects
 736 1, 7 and 8. The composite plume size-distribution for both Flight b622 and b623 is seen in Figure 5.

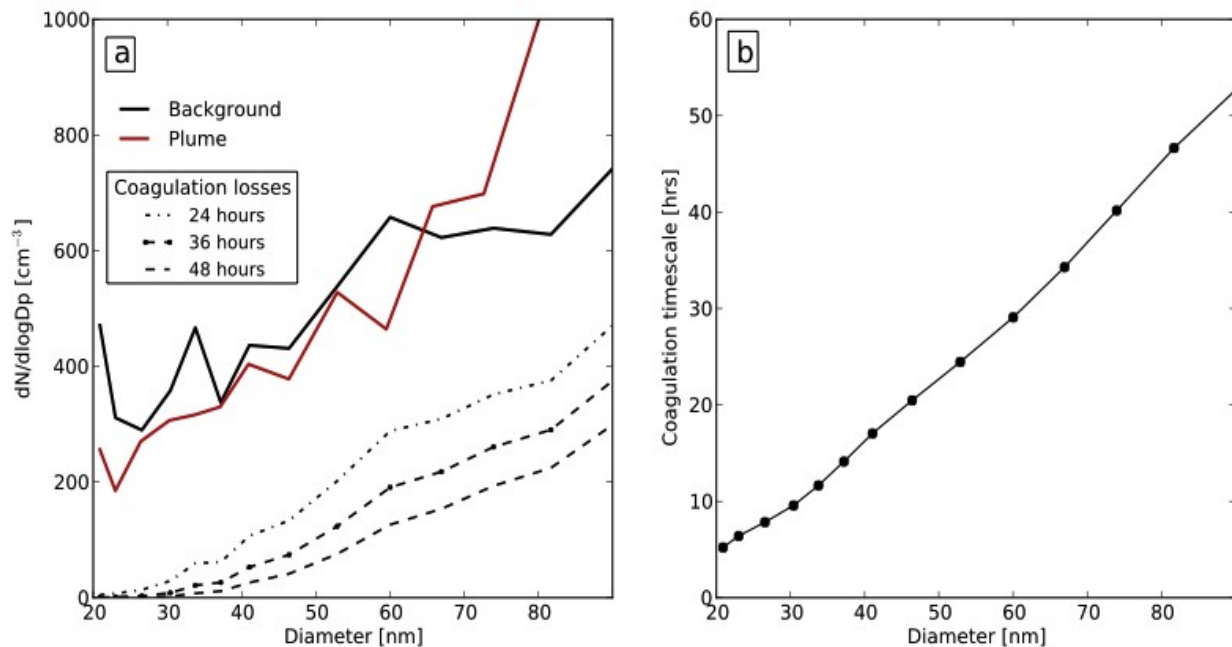


737 **Figure 4.** Accumulation mode peak diameter by transect (2-6, 9) showing no significant trend with
 738 plume transport distance. All colours are the same as in Figure 3. Distance from fire sources was
 739 estimated using transect midpoints and approximate source region area. Transects 1, 7 and 8 have
 740 insufficient accumulation mode plume data and have been omitted. The uncertainty bars show
 741 uncertainty in the distance from the source (± 150 km).

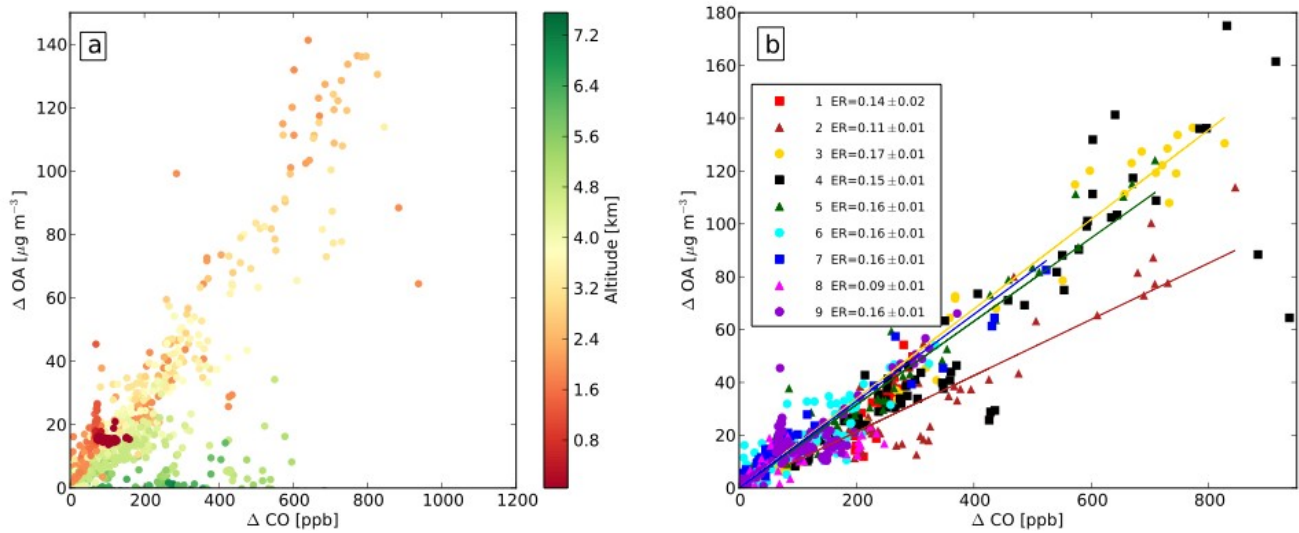
742
 743
 744
 745
 746
 747
 748
 749
 750
 751
 752
 753
 754
 755
 756



761 **Figure 5.** Composite median number size distributions for Flights b622 and b623 (cm⁻³ at STP). The
 762 in-plume (red) and background (grey) air distributions are shown as absolute concentrations (5a). The
 763 in-plume distributions are also normalized by CO mixing ratio (5b). The black lines are the median
 764 with the 25th and 75th percentiles overlain. The plume distributions have $D_{pm} = 230$ nm.



766 **Figure 6.** Figure 6a shows background (black solid line) and plume (red line) median concentrations
 767 for small particle diameters (20-90 nm). The black dashed lines are the number distributions after 24,
 768 36 and 48 hours of coagulation losses by the plume accumulation mode (Figure 5a) from the
 769 background level concentrations. These calculated concentrations are much lower than those found in
 770 plume. Figure 6b shows the coagulation lifetime as a function of particle diameter (on the order of 10s
 771 of hours in this diameter range).



773 **Figure 7.** Enhancement ratios of $\Delta\text{OA}/\Delta\text{CO}$ for Flight b622. Figure 7a is coloured by altitude showing
 774 potential aerosol washout in the high-altitude plume (>4.6 km). Figure 7b shows the ERs separated by
 775 flight transect showing individual enhancement ratios of between 0.095 - $0.178 \pm 0.01 \mu\text{g m}^{-3} \text{ppb}^{-1}$ with
 776 generally high correlation coefficients ($R^2 > 0.7$) for the majority. The data points collected at altitudes
 777 greater than 4.6 km have been removed (as per 7a).

778
 779
 780
 781
 782
 783
 784
 785
 786
 787
 788
 789
 790
 791
 792
 793
 794
 795
 796
 797
 798
 799
 800
 801
 802

803
804
805
806
807
808
809
810
811
812
813
814
815
816
817
818
819
820
821
822
823
824
825

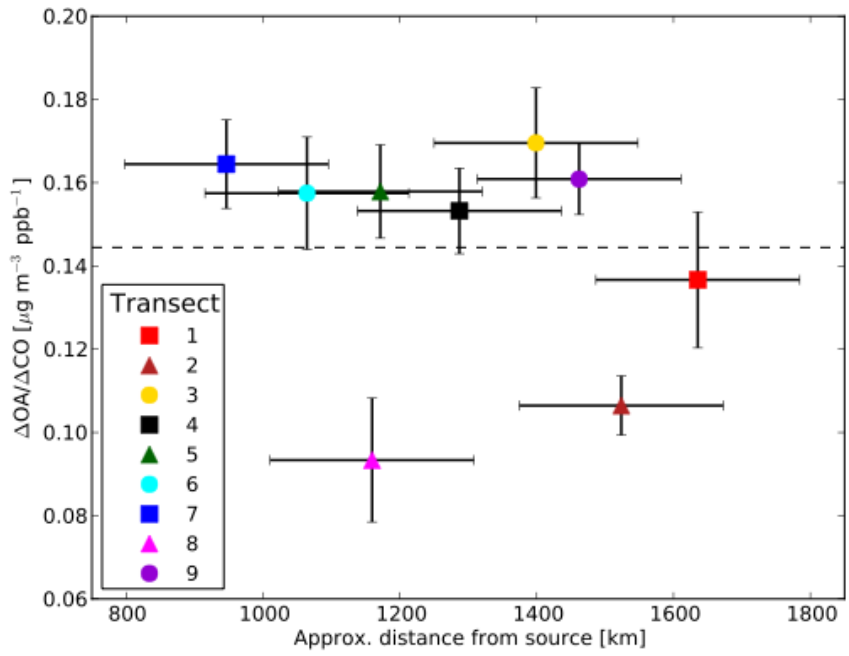
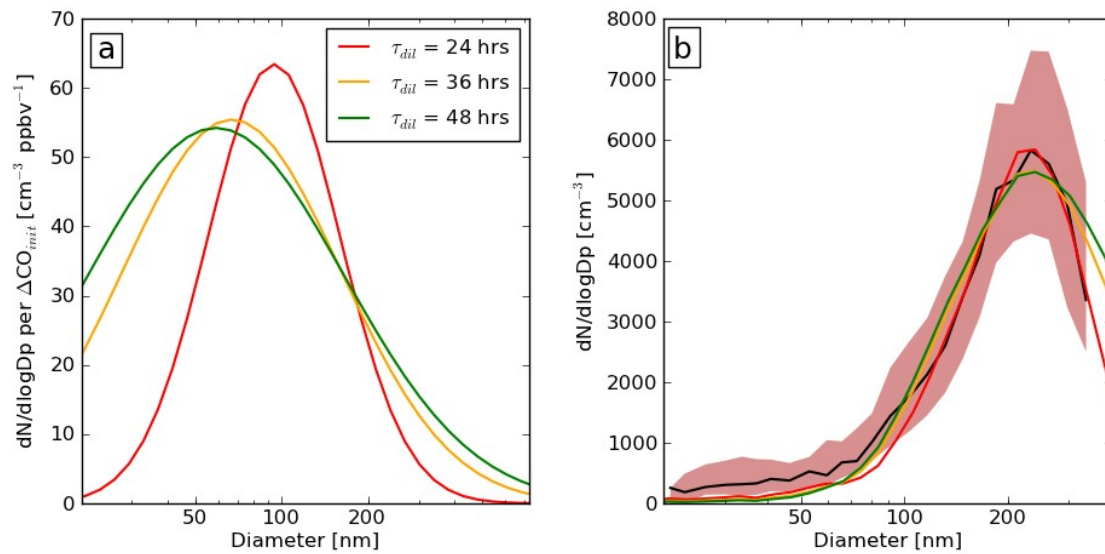
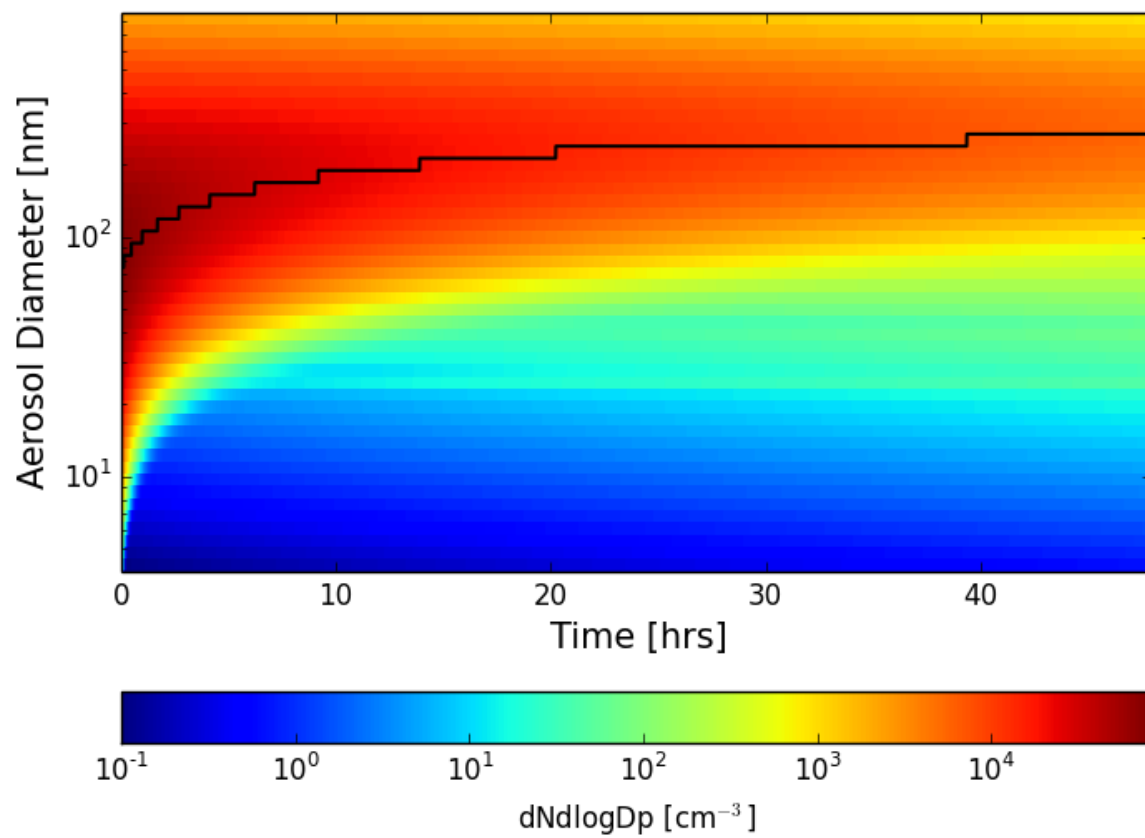


Figure 8. Transect $\Delta OA/\Delta CO$ enhancement ratios for Flight b622 as a function of the distance from the source fire region. The average ER is represented by the dashed black line ($0.1434 \mu g m^{-3} ppb^{-1}$). There is no discernible trend in ΔOA enhancement either by distance (x-axis) or time (colours). The uncertainty bars display the uncertainty in distance and in fitted enhancement ratios.



827 | **Figure 9.** Figure 9a shows the optimized [young-fresh-plume size-distributions](#) for entrainment
 828 | parameters $\tau_{dil} = 24, 36, 48$ hrs [as particle concentration per \$\Delta CO_{init}\$ \[\$cm^{-3}\$ ppbv \$^{-1}\$ \]](#). Figure 9b shows the
 829 | final modelled size-distributions compared to the measured aged plume size-distribution (black median,
 830 | red quartiles).



832 **Figure 10.** Plot of modelled size-distribution evolution for $\tau_{\text{dil}} = 36$ hrs. The black line shows the peak
 833 | diameter at each timestep ($\Delta t = 10$ s). The [youngfresh](#)-plume size-distribution has optimal initial
 834 | parameters: $D_{\text{pm}}=67$ nm, $\sigma=2.4$, $N_0 = 80,000$ cm^{-3} .